# Superconducting Magnetic Energy Storage Modeling and Application Prospect

**Jian-Xun Jin and Xiao-Yuan Chen**

**Abstract** Superconducting magnetic energy storage (SMES) technology has been progressed actively recently. To represent the state-of-the-art SMES research for applications, this work presents the system modeling, performance evaluation, and application prospects of emerging SMES techniques in modern power system and future smart grid integrated with photovoltaic power plants. A novel circuit-field-superconductor coupled SMES energy exchange model is built and verified to bridge the applied superconductivity field to the electrical engineering and power system fields. As an emerging SMES application case to suit photovoltaic power plants, a novel low-voltage rated DC power system integrated with superconducting cable and SMES techniques is introduced and verified to implement both the high-performance fault current limitation and transient power buffering functions. Four principal SMES application schemes of a sole SMES system, a hybrid energy storage system (HESS) consisting of small-scale SMES and other commercial energy storage systems, a distributed SMES (DSMES) system, and a distributed HESS (DHESS) are proposed and compared for achieving efficient and economical power management applications in future photovoltaic power plants.

**Keywords** Energy storage · Superconducting magnetic energy storage · Energy exchange modeling · Superconducting AC loss · Circuit-field-superconductor coupled analysis · Microphotovoltaic grid · Smart grid

J.-X. Jin (✉)
School of Electrical Engineering and Automation, Tianjin University, Tianjin, China
e-mail: jxjin@tju.edu.cn

X.-Y. Chen
School of Engineering, Sichuan Normal University, Chengdu, China



M.R. Islam et al. (eds.), *Advances in Solar Photovoltaic Power Plants*,
Green Energy and Technology, DOI 10.1007/978-3-662-50521-2_10

## 1 Introduction to Energy Storage

The alternatives for the continued availability of highly reliable and inexpensive power supply in future smart grid include the deployment of clean coal generation, nuclear power generation, renewable energy generation, and other generation resources. It is expected to combine with centralized and distributed power generation for developing the modern resource-saving and environment-friendly power systems. The main role of the energy storage systems (ESSs) is to increase the penetration of renewable energy sources such as photovoltaic power plants, to level the load curve, to contribute to the frequency control, to upgrade the transmission line capability, to mitigate the voltage fluctuations, and to increase the power quality and reliability, etc. Various ESSs can be used to allow increased capacity and stability to be derived from any given quantity of physical resources like photovoltaic power plant, and should be considered as a strategic choice that allows for optimum use of existing and new resources of all kinds [1–6].

According to the energy forms of the currently available ESSs, they are mainly divided into chemical energy storage and physical energy storage, as shown in Fig. 1. For the chemical energy storage, the mostly commercial branch is battery energy storage, which consists of lead-acid battery, sodium-sulfur battery, lithium-ion battery, redox-flow battery, metal-air battery, etc.

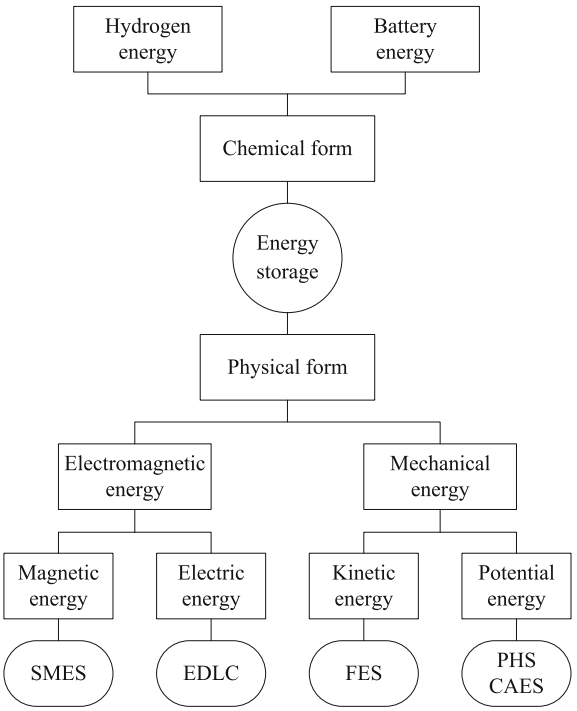


**Fig. 1** Classification of energy storage systems

The use of lead-acid batteries for energy storage dates back to mid-1800s. Lead-acid battery consists of spongy lead as the negative active material, lead dioxide as the positive active material, immersed in diluted sulfuric acid electrolyte, and lead as the current collector. It is most widely used due to its low capital cost and mature production techniques; however, it also has serious shortcomings such as low storage efficiency and performance degradation under the fast repeated charge–discharge operations.

Sodium-sulfur battery consists of molten sulfur at the positive electrode and molten sodium at the negative electrode separated by a solid beta alumina ceramic electrolyte. It is known for its strong cycle life, decent energy efficiency, and specific energy 3–4 times that of lead-acid battery. Moreover, it is able to provide short power bursts (about 30 s) that are 6 times of the rated continuous power, making it particularly suitable in short-time power quality maintenance.

Lithium-ion battery is a typical new-type high-energy and high-efficiency batteries. Its positive electrode is made of a lithium metal oxide, and the negative electrode is composed of layered graphitic carbon. Thanks to its extremely high efficiency as well as high energy density, power density, cell voltage, and long cycle life over other batteries, lithium-ion battery has become popular in various advanced equipment applications such as electric vehicle, computer, and cell phone. However, its special packaging of overcharge protection circuit causes the high production cost, which eventually prevents many large-scale systems from being developed and industrialized.

Another promising environment-friendly hydrogen energy storage branch has three fundamental forms of compressed gaseous hydrogen ($CGH_2$), liquid hydrogen ($LH_2$), and solid-state absorbers [7, 8]. The mostly commercial $CGH_2$ is operated at 35–70 MPa and room temperature, while the promising $LH_2$ with much higher energy density and no high-pressure risk is operated at 0.5–1 MPa and 20–30 K. The solid state absorbers of hydrogen include hydrides and high-surface materials, which offer very high volumetric hydrogen density on a materials basis.

The physical energy storage can be further divided into mechanical energy storage and electromagnetic energy storage. Among the mechanical energy storage systems, there are two subsidiary types, i.e., potential-energy-based pumped hydro storage (PHS) and compressed air energy storage (CAES), and kinetic-energy-based flywheel energy storage (FES).

Pumped hydro storage system consists of two reservoirs with a height differential and a penstock or pipe connecting them. To produce electrical energy, water is allowed to flow from the upper reservoir down the pipe through a water turbine and into the lower reservoir. Its simplicity of design, relatively low cost, and similarity in operation to hydroelectric power has made it the industry standard for storage for a century. However, its practical installation requires very specific geographic conditions and high capital cost, and might cause some undesirable environmental impacts.

Compressed air energy storage system consists of air compressor, air recuperator, and air storage place, which can be in a geologic formation such as salt caverns from mining, impervious rock formations, porous rock aquifers, and depleted oil or

gas wells. Once the air is compressed and stored, electrical energy is extracted using a standard gas turbine. Thanks to its similarity to standard combustion turbine systems, compressed air energy storage systems are easily integrated into the existing power systems.

Flywheel energy storage system stores kinetic energy in a rotatory disc in the form of angular momentum. It has high power density, high energy density, and virtually infinite number of charge–discharge cycles. Recent advances in power electronics and bearing material engineering have made this technology attractive for a number of other applications such as frequency regulation and power quality improvement. Moreover, the promising superconducting suspended bearings have significantly reduced the self discharge due to the frictional losses.

In practice, the electromagnetic energy storage systems consist of electric-energy-based electrochemical double-layer capacitor (EDLC), which is also called super capacitor or ultra capacitor, and magnetic-energy-based superconducting magnetic energy storage (SMES).

Electrochemical double-layer capacitor uses high-permittivity dielectric with a very high electrode surface area. The electrode surface area is maximized by using porous carbon as the current collector, allowing a relatively large amount of energy to be stored at the collector surface. The two electrodes are separated by a very thin porous separator and immersed in an electrolyte such as propylene carbonate. Electrochemical double-layer capacitor has the ability to charge and discharge more quickly over electrochemical batteries, and can practically be charged at any rate within an available temperature range from about −55 to 85 °C. However, due to the high permeability and close proximity of the electrodes, EDLC has a low-voltage-withstand capability, e.g., 2–3 V. This can be a serious problem to achieve the current and voltage balances within the hundreds to thousands of series-parallel-connected EDLC units for high-voltage applications.

Superconducting magnetic energy storage system can store electric energy in a superconducting coil without resistive losses, and release its stored energy if required [9, 10]. Most SMES devices have two essential systems: superconductor system and power conditioning system (PCS). The superconductor system mainly consists of (i) superconducting magnet (SM), (ii) cryogenic Dewar, (iii) refrigeration system, (iv) quench protection system, (v) persistent current switch, and (vi) current leads. The PCS mainly consists of (i) current-voltage (I-V) chopper, (ii) DC-link capacitor, (iii) DC-AC bidirectional converter, and (iv) AC filter. As compared to other ESSs, it has advantages: (i) fast response speed, (ii) high power density, (iii) high storage efficiency, (iv) long life-time, and (v) little environmental pollution. In addition, several subsidiary benefits from the SMES technology can be also derived (i) to lower the consumption of fossil resources, (ii) to increase the operation efficiency and lifetime of generators, (iii) to defer the power generation and transmission capacities, and (iv) to increase the availability of renewable energy sources such as photovoltaic power plants.

## 2 SMES Modeling and Verification

### 2.1 Energy Exchange Circuit

The PCSs for SMES applications mainly include [11–14] thyristor-based, current source converter (CSC-based, and voltage source converter (VSC)-based topologies, which can be used to develop various power conversion, compensation, and control equipments, e.g., (i) flexible AC transmission systems (FACTS) for power transmission, (ii) distributed FACTS (DFACTS) for power distribution, and (iii) uninterrupted power supplies (UPSs) for power end-users.

Figure 2 shows a typical VSC-based PCS. It mainly includes an SM in the cryostat, a current/voltage (I/V) chopper, a DC-link capacitor, a DC/AC converter, and an AC filter. The PCS can be connected in series or in parallel with the AC grid. Figure 3 shows three basic FACTS and DFACTS schemes, i.e., (i) series-type static synchronous series compensator (SSSC), (ii) parallel-type static synchronous compensator (STATCOM), and (iii) series-parallel-type unified power flow controller (UPFC) formed by the combination of a SSSC and a STATCOM. For the applications in high-voltage alternating-current (HVAC) and high-voltage direct-current (HVDC) transmissions, large-scale PCSs consisting of multilevel choppers and converters are needed. In various DC applications such as DC output-type distributed generators and DC distribution network, the SMES has

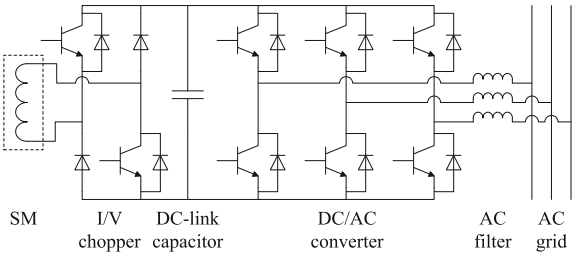


**Fig. 2** Topology of a typical VSC based PCS

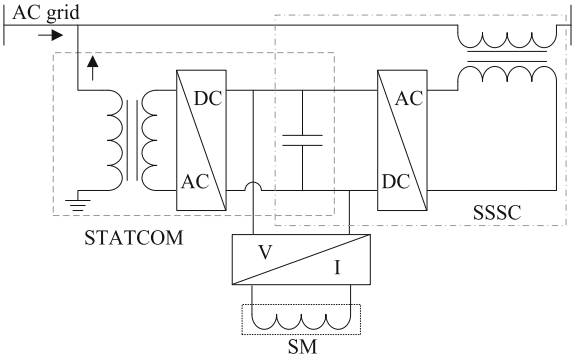


**Fig. 3** Topologies of three basic FACTS and DFACTS schemes

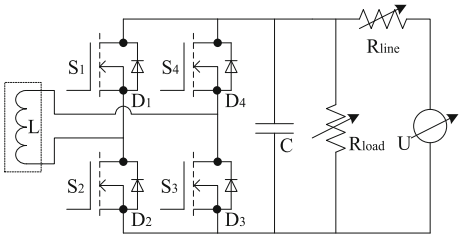


**Fig. 4** Energy exchange circuit with a brige-type chopper

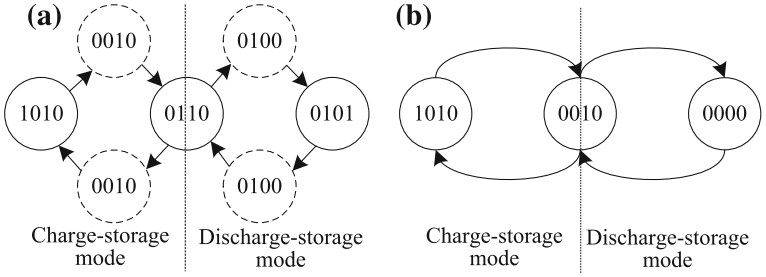


**Fig. 5** Digital state diagrams of the two I-V choppers: **a** Bridge-type chopper; **b** Conventional chopper

simpler system topology and easier control requirement. Only an I/V chopper is needed to link the SC to the DC bus for online power flow regulation.

For the SM used in a SMES device, the targeted power system applications can be transformed into equivalent energy exchange demands. To simplify the relatively complex system topology and relevant control strategies, an equivalent load network is therefore introduced to build an energy exchange circuit, as shown in Fig. 4 [15–18]. A controllable voltage source $U$ is used to imitate the external power fluctuations, a power-line resistor $R_{\text{line}}$ is used to imitate the consumed power from the step-up power transformer, AC filter, and DC/AC converter in a practical PCS, while a power-load resistor $R_{\text{load}}$ is used to imitate the external load fluctuations. To maintain the voltage $U_{\text{R}}(t)$ across the power-load resistor around its rated voltage, the SM should carry out the dynamic energy exchanges through the online conversions of the operation state of the chopper used. Thus, the external power system problems to be solved can be equivalently achieved by adjusting the above three controllable parameters.

As for the energy exchange control, a bridge-type I-V chopper formed by four MOSFETs $S_1$–$S_4$ and two reverse diodes $D_2$ and $D_4$ is introduced [15–18]. By defining the turn-on or turn-off status of a MOSFET as "1" or "0," all the operation states can be digitalized as "$S_1S_2S_3S_4$." As shown in Fig. 5, the charge-storage mode ("1010" → "0010" → "0110" → "0010" → "1010") and the discharge–storage mode ("0101" → "0100" → "0110" → "0100" → "0101") correspond to

the control schemes for the power absorption operation and the power compensation operation, respectively. To carry out the comparative analyses, two MOSFETs $S_1$ and $S_3$ and two reverse diodes $D_2$ and $D_4$ are also introduced to form a conventional chopper.

When the operation voltage $U_R(t)$ across the power-load resistor $R_{load}$ is between a minimum reference voltage $U_{min}$ and a maximum reference voltage $U_{max}$, i.e., $U_{min} \leq U_R(t) \leq U_{max}$, the power-load resistor is assumed to operated in a rated voltage state, and thus the I-V chopper is operated in the energy storage state. The system current and voltage equations can be expressed by

$$U = I(t)R_{line} + I_R(t)R_{load} \tag{1}$$

$$U_0 + \frac{1}{C}\int_0^t I_C(t)\mathrm{d}t = I_R(t)R_{load} \tag{2}$$

$$I(t) = I_R(t) + I_C(t) \tag{3}$$

where $I(t)$, $I_R(t)$, and $I_C(t)$ are the currents through the power-line resistor, power-load resistor, DC-link capacitor and SM; $U_0$, the initial voltage across the power-load resistor and DC-link capacitor; $C$, the capacitance of the DC-link capacitor.

When $U_R(t) > U_{max}$, the power-load resistor is operated in a voltage swell state, and the I-V chopper is operated in the energy charge state. The system current and voltage equations can be expressed by (1), (4), and (5)

$$L\frac{\mathrm{d}I_L(t)}{\mathrm{d}t} + I_L(t)R_{SC} = U_0 + \frac{1}{C}\int_0^t I_C(t)\mathrm{d}t = I_R(t)R_{load} \tag{4}$$

$$I(t) = I_L(t) + I_R(t) + I_C(t) \tag{5}$$

where $L$ is the inductance of the SM; $I_L(t)$, the coil current; $I_0$, the initial coil current; $R_{SC}$, the equivalent lossy resistance, which mainly comes from the I-V chopper and current leads.

When $U_R(t) < U_{max}$, the power-load resistor is operated in a voltage sag state and the I-V chopper is operated in the energy discharge state. The system current and voltage equations can be expressed by (1), (6), and (7)

$$-L\frac{\mathrm{d}I_L(t)}{\mathrm{d}t} - I_L(t)R_{SC} = U_0 + \frac{1}{C}\int_0^t I_C(t)\mathrm{d}t = I_R(t)R_{load} \tag{6}$$

$$I(t) + I_L(t) = I_R(t) + I_C(t) \tag{7}$$

## 2.2 Superconducting AC Loss Calculation

The sample SC used is a 0.2 H Bi-2223 solenoid coil having three same axial coil units in series [15]. Each unit is wounded by 21 layers with 35 turns per layer. The average gap width between the adjacent units is about 6 mm. The average gap width between the adjacent layers in one coil unit is about 2.7 mm. A 2D axisymmetric simulation model is built by using COMSOL software, as shown in Fig. 6. It consists of 63 coil layer units, and each unit formed by 35 turns has radial width of 12.6 mm and axial height of 4.2 mm. The inner and outer radii of each unit are 68 and 80.6 mm, respectively. The Bi-2223 tapes used are the AMSC high-strength tapes, whose average width is—4.2 mm, average thickness—0.28 mm, critical current—145.8 A at 77 K and self field. The filamentary thickness $d_c$ and width $w_c$ are 0.18 and 3.8 mm. The perpendicular and parallel time constants $\tau_{\perp}$ and $\tau_{//}$ are 33.07 and 0.93 ms, respectively.

In the 0.2 H Bi-2223 coil, the parallel component accounts for the vast majority of the total magnetic field distributed in the inner cavity area. However, the perpendicular component becomes larger as the location gets closer to two coil ends, as shown in Fig. 7. Due to the anisotropy, the turns located at two coil ends have

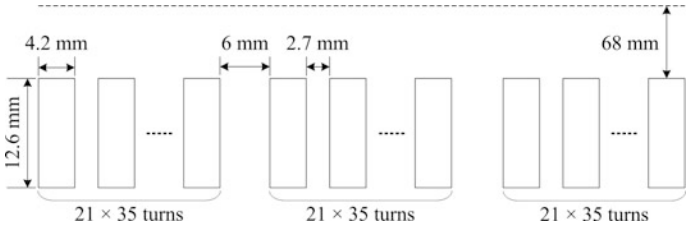


**Fig. 6** 2D axisymmetric model of the 0.2 H Bi-2223 solenoid coil

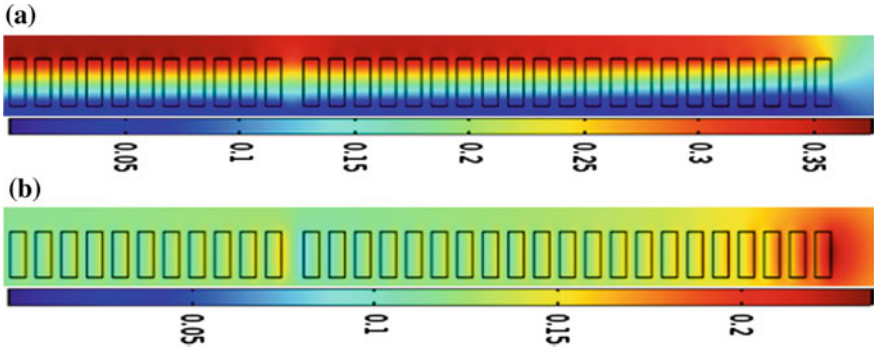


**Fig. 7** Magnetic field distributions of the 0.2 H Bi-2223 solenoid coil when $I(t)$ is 60 A: **a** parallel magnetic field; **b** perpendicular magnetic field

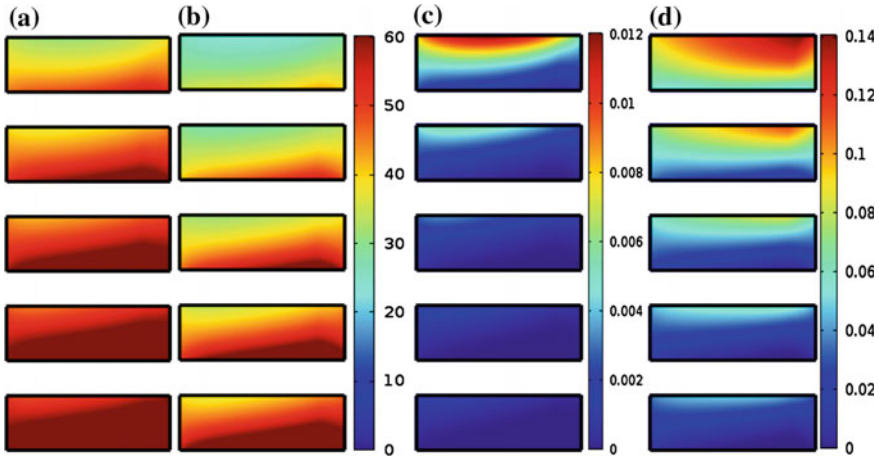


**Fig. 8** Critical current and flux flow loss distributions of the five upper coil layers: **a** critical current distributions when $I_L(t)$ = 40 A; **b** critical current distributions when $I_L(t)$ = 60 A; **c** flux flow loss distributions when $I_L(t)$ = 40 A; **d** flux flow loss distributions when $I_L(t)$ = 60 A

lower critical current and higher flux flow loss as compared to those located at the middle coil part. Figure 8 shows the critical current and flux flow loss distributions of the five upper coil layers. To make all the coil turns of the 0.2 H Bi-2223 coil work at superconducting state, the calculated $I_c(B_{//}, B_{\perp})$ is about 40 A.

Besides the mentioned flux flow loss above, the superconducting tapes in the SC will also generate a certain amount of hysteresis loss, coupling current loss, and eddy current loss due to the real-time changes of the coil current and magnetic field during the energy exchange operations.

From the top to bottom of the 63 coil layers, they are defined as $N_{layer}$ = 1, $N_{layer}$ = 2, …, $N_{layer}$ = 63, respectively. The top coil layer ($N_{layer}$ = 1) generates the maximum perpendicular hysteresis loss and perpendicular coupling current loss, while the middle coil layer ($N_{layer}$ = 32) generates the maximum parallel hysteresis loss and parallel coupling current loss, as shown in Figs. 9 and 10. The left side of each layer in Figs. 9 and 10 is located in the inner wall of the coil.

Based on the FEM calculations in Fig. 11, the total hysteresis loss $P_{hys}(t)$, flux flow loss $P_{flow}(t)$, coupling current loss $P_{coup}(t)$, and eddy current loss $P_{eddy}(t)$ can be fitted into four coil-current-dependent formula, as depicted by [19]

$$P_{hys}(t) = P_1 \times a_1 \times \left[\frac{I_m(t)}{I_1}\right]^{a_2} \times \frac{f(t)}{10 \times f_1} \tag{8}$$

$$P_{flow}(t) = P_1 \times b_1 \times \left[\frac{I_L(t)}{I_1}\right]^{b_2} \tag{9}$$

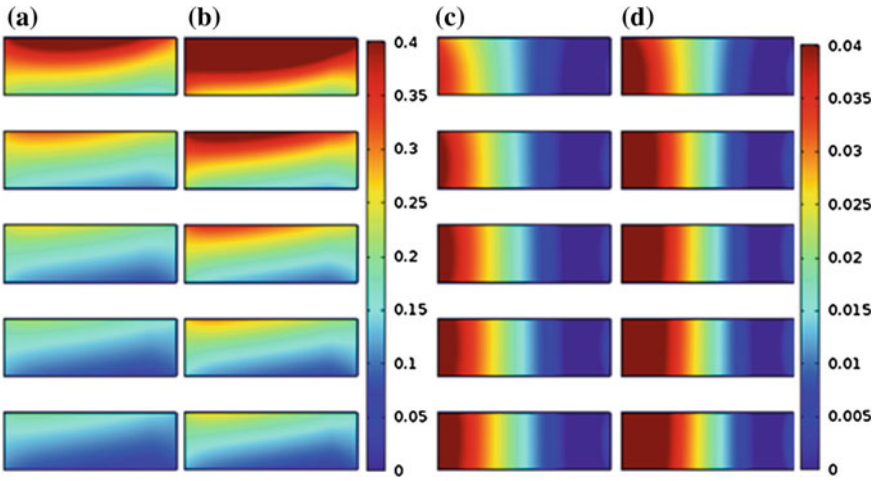


**Fig. 9** Perpendicular and parallel hysteresis loss distributions: **a** $P_{hys\perp}$, $N_{layer} = 1$ to $N_{layer} = 5$, $I_m = I_{dc} = 15$ A, $f = 10$ Hz; **b** $P_{hys\perp}$, $N_{layer} = 1$ to $N_{layer} = 5$, $I_m = I_{dc} = 20$ A, $f = 10$ Hz; **c** $P_{hys//}$, $N_{layer} = 30$ to $N_{layer} = 34$, $I_m = I_{dc} = 15$ A, $f = 10$ Hz; **d** $P_{hys//}$, $N_{layer} = 30$ to $N_{layer} = 34$, $I_m = I_{dc} = 20$ A, $f = 10$ Hz

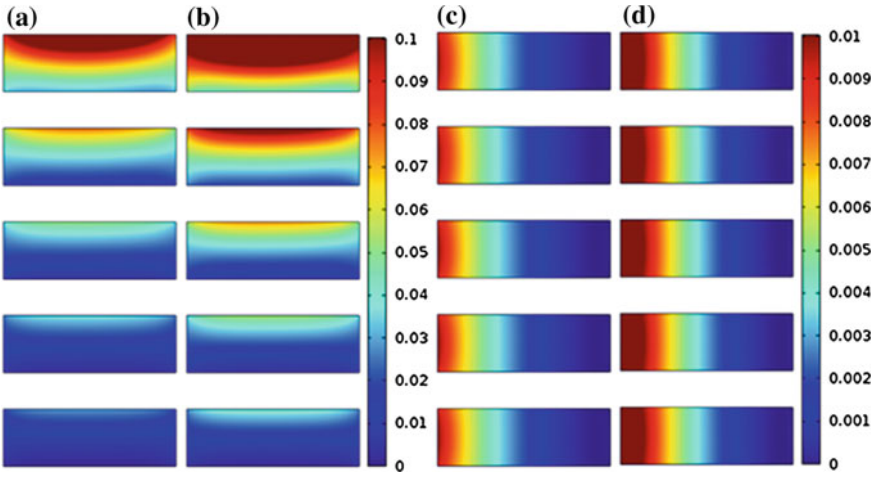


**Fig. 10** Perpendicular and parallel coupling current loss distributions: **a** $P_{coup\perp}$, $N_{layer} = 1$ to $N_{layer} = 5$, $S(t) = 50$ A/s; **b** $P_{coup\perp}$, $N_{layer} = 1$ to $N_{layer} = 5$, $S(t) = 60$ A/s; **c** $P_{coup//}$, $N_{layer} = 30$ to $N_{layer} = 34$, $S(t) = 50$ A/s; **d** $P_{coup//}$, $N_{layer} = 30$ to $N_{layer} = 34$, $S(t) = 60$ A/s

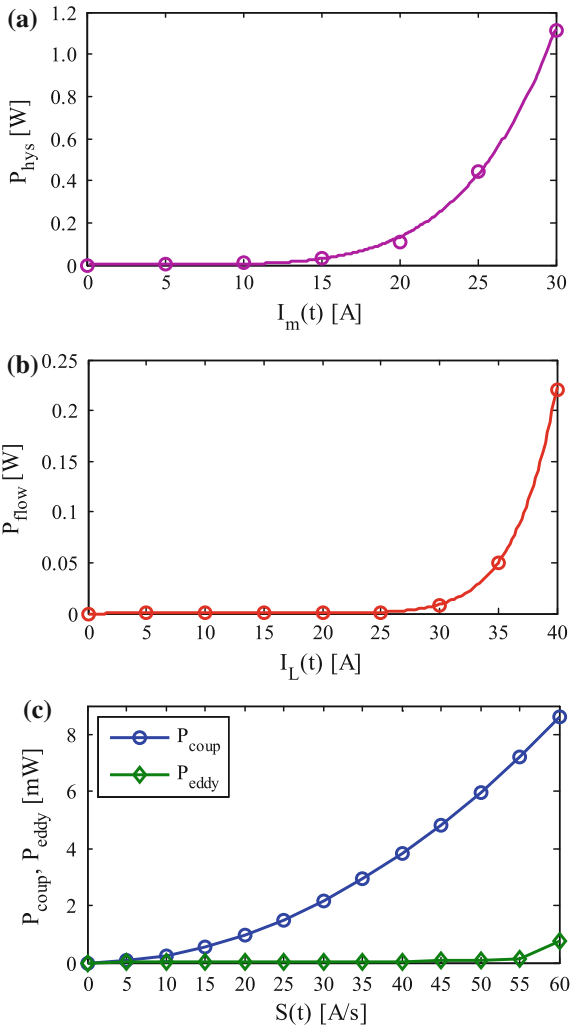


**Fig. 11** Calculated and fitted AC loss of the whole coil: **a** hysteresis loss; **b** flux flow loss; **c** coupling current loss and eddy current loss

$$P_{\text{coup}}(t) = P_1 \times c_1 \times \left[\frac{1}{60} \times \frac{S(t)}{S_1}\right]^2 \tag{10}$$

$$P_{\text{eddy}}(t) = P_1 \times d_1 \times \left[\frac{1}{60} \times \frac{S(t)}{S_1}\right]^2 \tag{11}$$

where $I_{\text{m}}(t)$ and $f(t)$ are the peak current and operation frequency of the AC coil current; $a_1$, $a_2$ $b_1$, $b_2$, $c_1$, $d_1$, the coil-structure-dependent parameters; $I_1$, $P_1$, $f_1$, $S_1$, the normalizing constants of 1 A, 1 W, 1 Hz, 1 A/s. For the 0.2 H Bi-2223 coil, the fitted parameters $a_1 = 1.841 \times 10^{-5}$, $a_2 = 5.269$, $b_1 = 3.048 \times 10^{-19}$, $b_2 = 11.151$, $c_1 = 8.61$, $d_1 = 0.75$.

According to (10) and (11), both the coupling and eddy current loss distributions are similar. It can be seen that the total coupling current loss is about 11.5 times of the total eddy current loss. When the current changing rate $S(t)$ = 60 A/s, the total coupling current loss is about 8.3 mW, while the total eddy current loss is only about 0.7 mW.

## 2.3 Circuit-Field-Superconductor Coupled Model

In the past decades, the researchers in the applied superconductivity field have developed a number of superconducting magnet (SM) models based on the numerical and finite element algorithms to calculate and optimize the AC loss features of the SM itself. Due to its relatively complex system topologies and control strategies of a practical PCS, the most models [20] employed simple triangle or trapezoid coil current waves, which are insufficient to match with the practical coil current waves with high precision under dynamic energy exchange operations. On the other side, the researchers in the electrical engineering field have developed a number of PCS models, in which the SM is just utilized as an ideal lossless inductor to evaluate the energy exchange performance for the external system [21, 22].

To have both the superconducting AC loss and energy exchange features integrated in one model, this work proposes a new superconducting magnetic energy exchange (SMEE) model based on a circuit-field-superconductor coupled method. The PCS is simplified into an equivalent energy exchange circuit model for use in the AC loss calculations, while the superconductor system provides a coil-current-dependent SM model for use in the energy exchange performance evaluations.

The four main AC losses of the SM in a SMES device are simply calculated by four coil-current-dependent formulas (8)–(11), while the real-time coil current is equivalently obtained by solving the system current and voltage equations (1)–(7) of the equivalent energy exchange circuit. Thus, the coil current can be served as an intermediate link to bridge the applied superconductivity field with the electrical engineering field.

The basic principle of the circuit-field-superconductor coupled analysis is shown in Fig. 12. The SM is controlled to carry out the bi-directional energy exchanges with the external system through the equivalent energy exchange circuit. These will

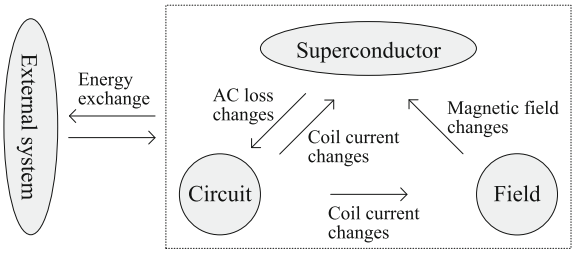


**Fig. 12** Principle of circuit-field-superconductor coupled method

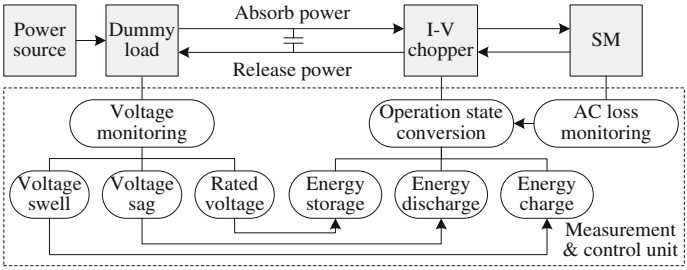


**Fig. 13** Scheme of the SMEE model

cause the real-time changes of the coil current in the SM, and thus generate the varying magnetic field around the SM. The changes of both the coil current and magnetic field result in varying AC losses and thus diminish the stored magnetic energy in the SM and its corresponding coil current.

Based on the circuit-field-superconductor coupled method, a new SMEE model is built, as shown in Fig. 13 [19]. It mainly consists of one controllable voltage source, one dummy load, one DC-link capacitor, one I-V chopper, one SM, and one measurement and control unit. The dummy load corresponds to the combination of the power-line resistor and power-load resistor in Fig. 4. The measurement and control unit is used to implement the online state conversion of the I-V chopper based on the power and voltage monitoring of the dummy load. In addition, an AC loss monitoring module is also added to limit the total AC loss $P_{ac}$ within the maximum cooling power $P_{max}$ in the practical refrigeration system. If the generated AC losses exceed the upper limitation in any case, the operation state of the I-V chopper should be converted into the energy storage state immediately to avoid the quench of the SM.

The SMEE model has the potentials to evaluate the AC loss features under a given energy exchange condition and to evaluate the energy exchange features with a designed or developed SM prior to its practical application. The main input parameters include: (i) Energy exchange parameters—$U$, $U_{min}$, $U_{max}$, $R_{line}$, $R_{load}$, $C$; (ii) SM parameters—$L$, $I_0$, $S_m$, $P_m$, $a_1$, $a_2$, $b_1$, $c_1$, $d_1$, $d_2$. The main output parameters include: (i) Energy exchange parameters—$U_R(t)$, $T_{ch}$, $T_{dis}$; (ii) SM parameters—$I_L(t)$, $I_m(t)$, $f(t)$, $S(t)$, $I_c(t)$, $P_{hys}(t)$, $P_{flow}(t)$, $P_{coup}(t)$, $P_{eddy}(t)$, $P_{ac}(t)$. $T_{ch}$, and $T_{dis}$ are the charging and discharging time durations from the initial coil current $I_0$ to a reference value.

## 2.4 Simulation Analysis

Based on the developed SMEE model, a Matlab/Simulink simulation model is built. The energy exchange circuit is used to simulate the buffering effects for compensating a voltage sag. The main simulation parameters are as follows: $U$ = 300 V,

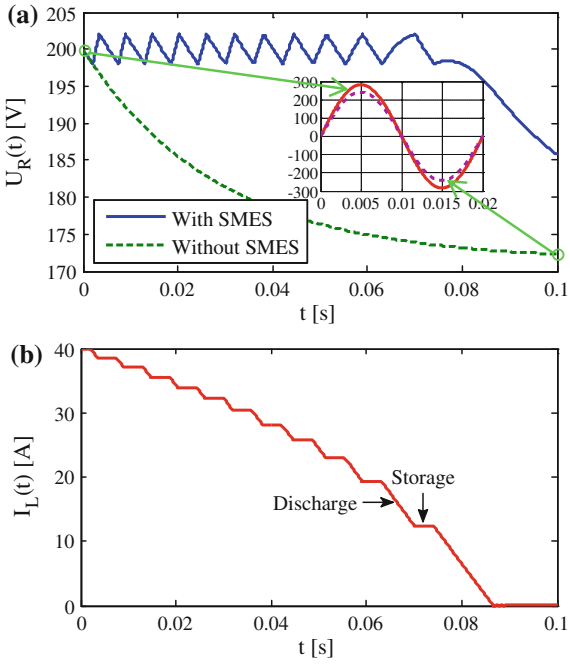


**Fig. 14** Simulated load voltage and coil current: **a** $U_R(t)$ versus $t$; **b** $I_L(t)$ versus $t$

$U_{max}$ = 202 V, $U_{min}$ = 198 V, $R_{line}$ = 5 Ω, $R_{load}$ = 20/3 Ω, $L$ = 0.2 H, $I_0$ = 40 A, and $C$ = 10 mH. The power-load resistor $R_{load}$ is assumed to converted from 10 to 20/3 Ω when the time $t$ = 0 s, thus the real-time load voltage $U_R(t)$ will drop gradually to about 171 V without SMES, as shown in Fig. 14a. It should be noticed that the above DC voltage sag corresponds to an AC voltage sag from $200\sqrt{2} \times \sin(2\pi ft)$ V to $171\sqrt{2} \times \sin(2\pi ft)$ V, as shown in the insertion of the Fig. 14a—red line and purple line, respectively. $f$ is the power frequency in the modern power systems, e.g., 50 or 60 Hz.

In the case of the 0.2 H/40 A SMES is applied, the operation state of the I-V chopper is converted between the energy discharge state and energy storage state to discharge the shortfall power from the power-load resistor. Thus $U_R(t)$ is kept within the voltage range from 198 to 202 V for 0.07 s, i.e., $T_{dis}$ = 0.07 s. This compensation time value is the same as that in the above equivalent AC voltage sag.

The four coil-current-dependent formulas are used to calculate the hysteresis loss, flux flow loss, coupling current loss, and eddy current loss. The whole coil current curve in Fig. 14b is equivalent to half a charge–discharge cycle with $f$ = 5.7 Hz and $I_{dc} = I_m$ = 20 A. The calculated hysteresis loss $P_{hys}$ and its generated energy consumption $Q_{hys}$ are about 60.4 mW and 5.2 mJ, respectively. Figure 15 shows the flux flow loss $P_{flow}$ and its generated energy consumption $Q_{flow}$ during the whole voltage sag compensation period. The generated energy consumption $Q_{flow}$ value is about 3.2 mJ.

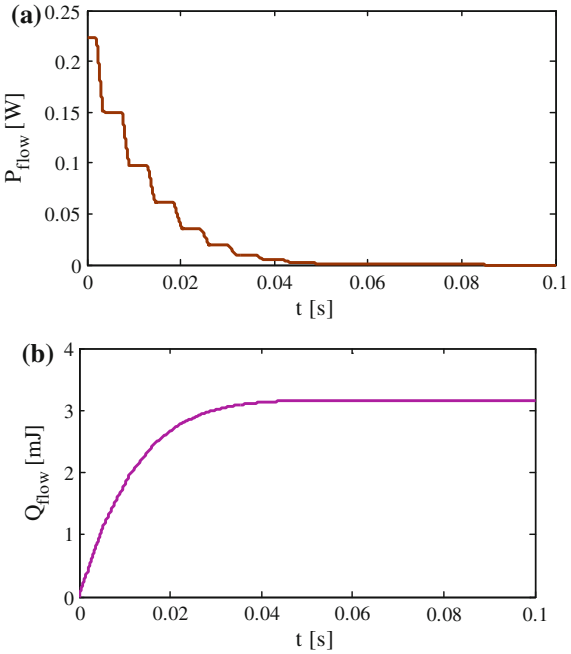


**Fig. 15** Simulated flux flow loss and energy consumption: **a** $P_{\text{flow}}(t)$ versus $t$; **b** $Q_{\text{flow}}(t)$ versus $t$

**Table 1** Simulation results for coupling and eddy current losses

| $I_{\text{L}}(t)$ (A) | $T_{\text{dis}}$ (ms) | $S(t)$ (A/s) | $P_{\text{coup}}$ (W) | $P_{\text{eddy}}$ (W) | $Q_{\text{coup}}$ (mJ) | $Q_{\text{eddy}}$ (mJ) |
|---|---|---|---|---|---|---|
| 40.0 | 1.378 | 1000.82 | 2.395 | 0.208 | 3.302 | 0.288 |
| 38.6 | 1.444 | 1000.81 | 2.395 | 0.208 | 3.459 | 0.301 |
| 37.2 | 1.517 | 1000.80 | 2.395 | 0.208 | 3.635 | 0.317 |
| 35.6 | 1.613 | 1000.79 | 2.395 | 0.208 | 3.864 | 0.337 |
| 34.1 | 1.724 | 1000.79 | 2.395 | 0.208 | 4.130 | 0.360 |
| 32.2 | 1.873 | 1000.79 | 2.395 | 0.208 | 4.487 | 0.391 |
| 30.4 | 2.054 | 1000.79 | 2.395 | 0.208 | 4.922 | 0.429 |
| 28.2 | 2.341 | 1000.83 | 2.395 | 0.208 | 5.608 | 0.489 |
| 25.8 | 2.774 | 1000.90 | 2.396 | 0.208 | 6.648 | 0.579 |
| 23.0 | 3.605 | 1001.11 | 2.397 | 0.209 | 8.641 | 0.753 |
| 19.4 | 6.968 | 1002.69 | 2.404 | 0.209 | 16.755 | 1.460 |
| 12.4 | 12.555 | 986.85 | 2.329 | 0.203 | 29.243 | 2.547 |

Table 1 shows the simulation results for the coupling and eddy current loss calculations. The coil current decreases gradually while the discharge time $T_{\text{dis}}$ in one energy discharge state increases for achieving the condition of 198 V ≤ $U_{\text{R}}(t)$ ≤ 202 V. During the 11 discharge–storage cycles in Fig. 14b, the total energy consumption $Q_{\text{coup}}$ from the coupling current loss and total energy

consumption $Q_{eddy}$ from the eddy current loss are 65.4 and 5.7 mJ, respectively. In the following energy discharge period from 12.4 to 0 A, they are 29.2 and 2.5 mJ, respectively.

## 2.5 Experimental Verification

Figure 16 shows the schematic diagram and overall experiment setup of the energy exchange prototype [15–17, 23]. Four OptiMOS™ MOSFETs are introduced to develop the bridge-type and conventional choppers, with the power lines among the four MOSFETs formed by silvered copper bars. The MOSFET parameters are as follows: drain-source breakdown voltage $V_{DSmax} = 30$ V, turn-on resistance $R_{on} \approx 0.65$ mΩ. Thirty-two conductive polymer aluminum solid electrolytic capacitors with ultra-low equivalent series resistance $R_{esr} \approx 11$ mΩ are connected in parallel to serve as the DC-link capacitor. The power-line resistor $R_{line}$ is combined by three independent 0.5 Ω resistors. The power-load resistor $R_{load}$ has three parallel resistor branches of $R_2$, $R_3$, and $R_4$. The available resistors in each branch are one 1 Ω resistor and two 2 Ω resistors. Each branch can be connected or disconnected to the power-line resistor by controlling its series-connected MOSFET. The high-temperature superconducting (HTS) coil is a 0.2 H Bi-2223 solenoid coil immersed in liquid nitrogen ($LN_2$). It consists of three solenoids in series for reducing the internal connections. The HTS coil is connected to the bridge-type chopper through two copper current leads. When the chopper is operated in the storage state, the total lossy resistance in series with the HTS coil is about 3.2 mΩ.

The main operation processes of the prototype are described as follows: (i) Close $S_1$, $S_3$ and $S_5$, the coil current $I_L(t)$ is firstly charged gradually to a pre-set initial current value $I_{L0}$. (ii) Open $S_1$, and then close $S_2$, the two choppers are operated in the storage state. (iii) Open $S_5$, and then close one, two or three branched MOSFETs of $S_6$–$S_8$, the corresponding branched resistors are connected to the controllable power source through the power-line resistor. (iv) Finally, a MCU MSP430 and CPLD EPM240 joint measurement and control module is to implement the online voltage monitoring of $U_R(t)$, and thus to change the next operation state of the choppers accordingly.

In the experiment, the controllable power source $U = 15$ V is first applied to the power-line resistor $R_1 = 0.5$ Ω and two branched power-load resistors $R_2 = R_3 = 1$ Ω. Each branched resistor is operated at its rated voltage $U_r = 10$ V. Assuming that one branch and three branches of $R_2 = R_3 = R_4 = 1$ Ω are connected with the power-line resistor successively, a voltage swell status and a voltage sag status will be appear accordingly. When the 0.2 H Bi-2223 coil is applied, it should be controlled to absorb a mean surplus power $P_{swell} = 100$ W and to compensate a mean shortfall power $P_{short} = 100$ W, respectively. As shown in Fig. 17, a whole 100 W energy exchange cycle can be divided into four different segments.

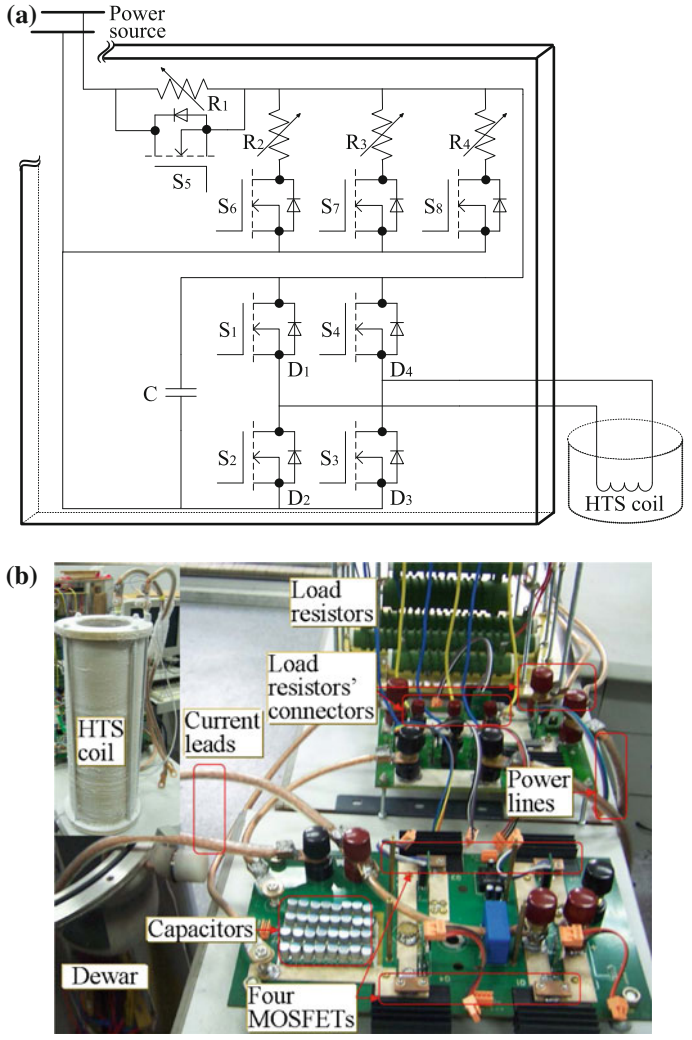


**Fig. 16** Developed SMES prototype: **a** schematic diagram; **b** experiment setup

The first one is an incomplete absorption segment when $I_L(t) < 10$ A, the two choppers are operated in the charge state until $U_R(t)$ drops to 10 V. The second one is a complete absorption segment when $10 \text{ A} \leq I_L(t) \leq 60$ A, the two choppers are operated in the charge storage mode to maintain $U_R(t)$ around 10 V. Once $I_L(t)$ reaches its rated operation current $I_{Lr} = 60$ A, the third process enters into a complete compensation segment. In this segment, the two choppers are operated in the discharge–storage mode to maintain $U_R(t)$ around 10 V until $I_L(t)$ drops to 10 A. The fourth one is an incomplete compensation segment when $I_L(t) < 10$ A, the two choppers are operated in the discharge state to release a decreasing power.

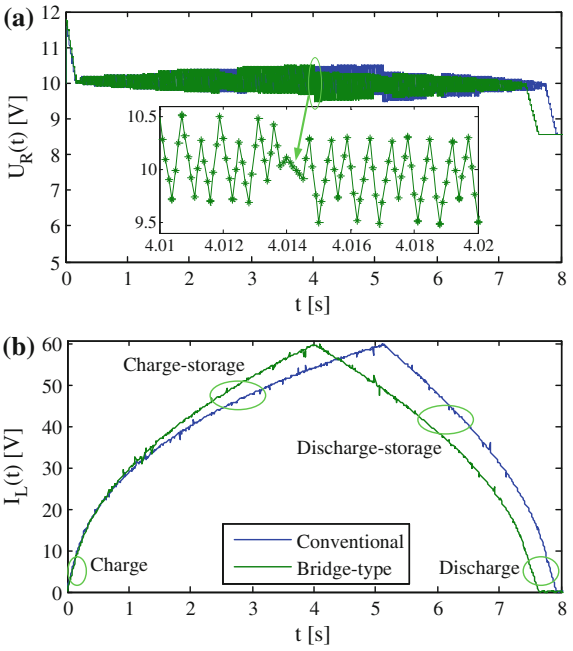


**Fig. 17** Measured results of $U_R(t)$ and $I_L(t)$ during a 100 W energy exchange cycle: **a** $U_R(t)$ versus $t$; **b** $I_L(t)$ versus $t$

To evaluate the performance of SMES before its practical applications, the surplus or shortfall power demands from the external system can be simply transformed into the combinations of $U$ and $R_1$—$R_4$. Thus the buffering effects of SMES for the given power fluctuations could be obtained equivalently in the above four segments.

Since the consumed power from the used OptiMOS™ MOSFETs is much lower over their reverse diodes [18], the bridge-type chopper has shorter absorption time $T_{abs}$ and longer compensation time $T_{com}$ as compared to the conventional one. This means that the bridge-type chopper has higher charge–discharge efficiency $\eta_{total}$, which is defined by $\eta_{total} = (P_{swell} \times T_{abs})/(P_{short} \times T_{com})$. From the measured results of Fig. 17, the $\eta_{total}$ values of the bridge-type and conventional choppers are about 0.876 and 0.526, respectively. Therefore, the bridge-type chopper is more suitable to apply in the low-voltage end-user applications for high-efficiency SMES operations. Figure 18a shows the measured and calculated results of $\eta_{total}$ versus $I_{L0}$. In the 100 W energy exchange cycle, $I_L(t)$ increases from $I_{L0}$ to 60 A, and then decreases from 60 A to $I_{L0}$. It can be seen that $\eta_{total}$ decreases along with the increment of $I_{L0}$. This is because the consumed power from the MOSFETs is in direct proportion to the square of the coil current. Figure 18b shows the measured and calculated results of $\eta_{total}$ versus $P_{ref}$. $P_{ref}$ is assumed to be equal to both the $P_{swell}$ and $P_{short}$. It can be seen that $\eta_{total}$ increases with a reduced rising slope as $P_{ref}$ increases.

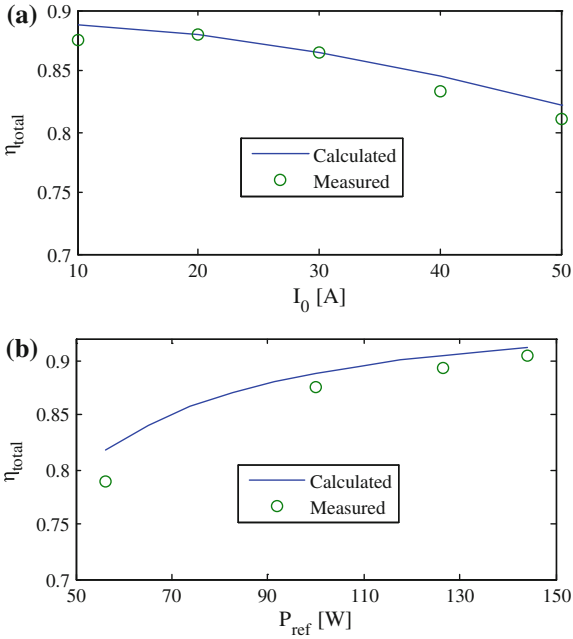


**Fig. 18** Measured and calculated results of $\eta_{total}$ during a 100 W energy exchange cycle: **a** $\eta_{total}$ versus $I_0$; **b** $\eta_{total}$ versus $P_{ref}$

Besides the independent charge and discharge tests, the prototype can also be used to carry out multicycle energy exchange tests to simulate a variety of application conditions. Figure 19a, b shows the measured results of $U_R(t)$ and $I_L(t)$ during five charge–discharge cycles. The 0.2 H Bi-2223 coil is applied to absorb a mean surplus power $P_{swell}$ = 100 W during the first half cycle, and then to compensate a mean shortfall power $P_{short}$ = 100 W during the residual half cycle.

Due to the energy consumptions from the conduction losses of the MOSFETs and magnetization loss of the Bi-2223 coil itself, $I_L(t)$ decreases continuously after each charge–discharge cycle. From Fig. 19b, $I_L(t)$ at the ends of the first cycle to fifth cycle are reduced to 24.78, 19.66, 13.69, 5.74, and 0.21 A, respectively. It is noticed that an incomplete compensation segment and an incomplete absorption segment appear successively within the time range from about 19.91 to 20.09 s. The corresponding lowest and highest offset voltage values are about 9.41 and 10.72 V, respectively.

Figure 19c, d shows the total AC loss $P_{mag}(t)$ and energy consumption $Q_{mag}(t)$. The calculated root-mean-square (RMS) values from the first cycle to fifth cycle are 1.21, 0.78, 0.52, 0.36, and 0.26 W, respectively. The corresponding $Q_{mag}(t)$ values are 6.02, 9.92, 12.53, 14.35, and 15.66 J, respectively.

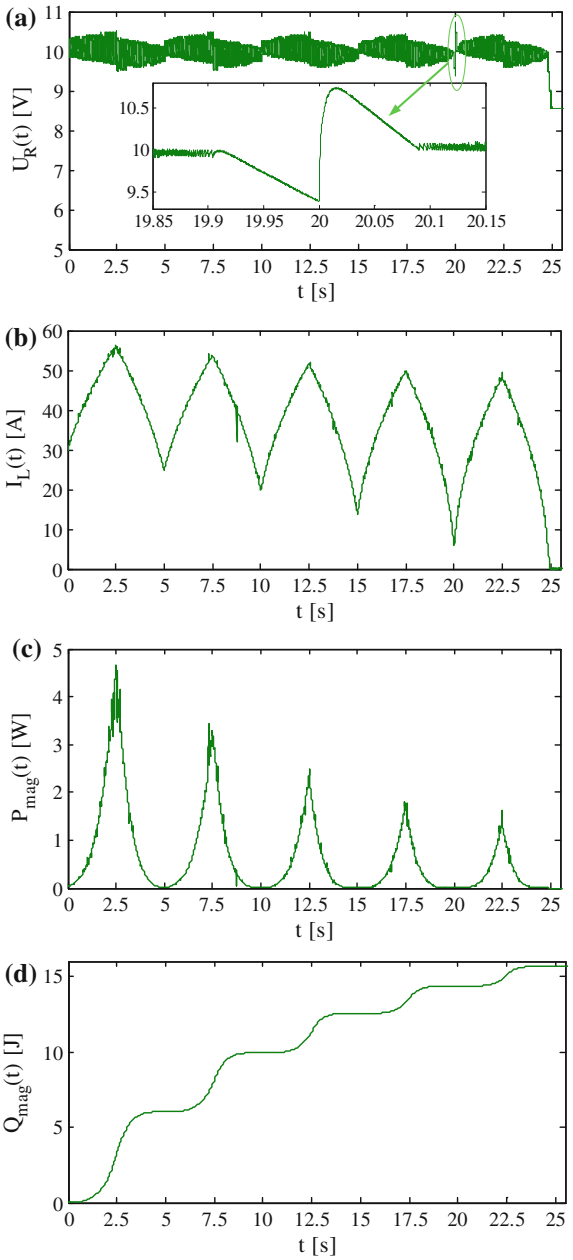


**Fig. 19** Measured and calculated results during five 100 W energy exchange cycle: **a** $U_R(t)$ versus $t$; **b** $I_L(t)$ versus $t$; **c** $P_{mag}(t)$ versus $t$; **d** $Q_{mag}(t)$ versus $t$

# 3 SMES-Based Microphotovoltaic Grid

## *3.1 Principle and System Description*

Due to the energy intermittency from the photovoltaic power plants, various energy storage systems are utilized to allow increased power capacity and stability. As compared to other energy storage schemes, emerging SMES technique is significantly highlighted for fast speed response and high power density. A number of SMES devices and systems have been studied and verified to apply in the modern power systems with or without the penetrations of the photovoltaic power plants [11–14, 24–26].

In addition, superconducting cables (SCs) are with the advantages of high transport current capability, no resistive loss and compact system, therefore high-power and high-efficiency transmissions for delivering the electric power directly from distant photovoltaic power plants to local power consumers can be achieved [27–29]. Besides the high-capacity electricity transmission, the SC can also serve as a self-acting fault current limiter for its power system auto protection because its resistance characteristic is similar to that in a resistive-type superconducting fault current limiter. Based on the self-acting fault-current-limiting (FCL) feature, the so-called FCL SC can achieve favorable grounding fault current limitation effect; meanwhile, it also has the significant potential to enhance the fault ride-through (FRT) capability of all the in-grid photovoltaic power plants.

To integrate the self-acting FCL feature from the FCL SC and the fast-response grid voltage protection feature from the SMES in one power system, this work proposes a novel low-voltage direct-current (LVDC) micro photovoltaic grid by applying multiple FCL SCs and SMES devices [30, 31]. The concept to form the novel LVDC microphotovoltaic grid is to implement the hybrid energy transfer of the hydrogen and electricity. As shown in Fig. 20, the most generated electricity from the photovoltaic power plants and utility grid supplies the distant power loads, while the surplus electricity produces the $LH_2$ by using water electrolyzers and liquefying devices. For the SC system, a main FCL SC is used to transfer the electricity to local residential and industrial areas, while multiple branch FCL SCs are used to distribute the electricity to various distributed loads.

For the SMES system, it can be divided into three different types: (i) The first type connected with the photovoltaic power plants is used to locally compensate the transient output power and voltage fluctuations; (ii) The second type connected with the AC loads, DC loads, and electric vehicles (EVs) is used to serve as fast-response uninterruptible power supplies (UPSs) for improving the local power quality; (iii) The third type connected with the bus line between the main FCL SC and multiple branch FCL SCs is used to bridge the photovoltaic power plants with various distributed loads, and thus to buffer the power and voltage fluctuations from the photovoltaic power plants and to compensate the load fluctuations from the distributed loads.

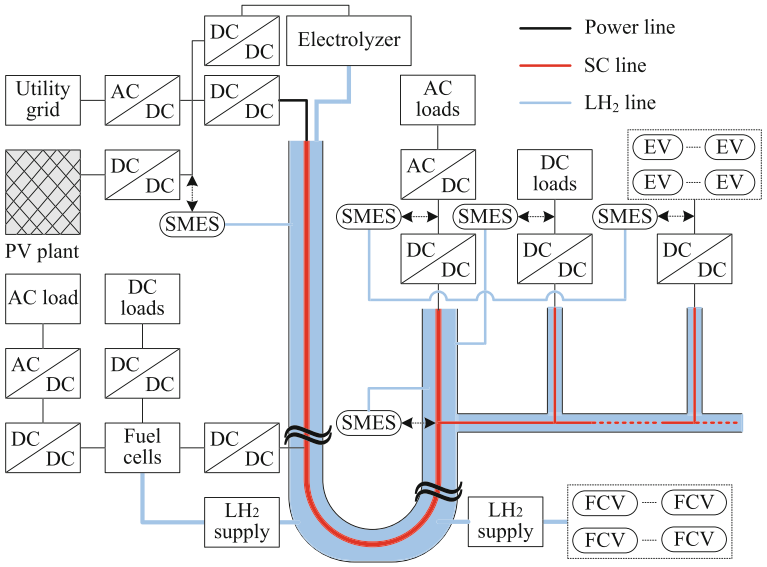


**Fig. 20** Sketch of the LVDC micro photovoltaic grid

As an alternative cooling method, the $LH_2$ transferred can not only be used to provide hydrogen energy for the fuel cells (FCs) and FC vehicles (FCVs), but also can be used as the refrigeration fluid for cooling the FCL SC and SMES systems. In addition to supply the off-grid AC and DC loads, the generated electricity from the FCs can also provide demanded power feedback to the LVDC network.

## *3.2 Simulation Model and Implementation*

To evaluate the performance of the integrated FCL SC and SMES systems during a grounding fault, a simulation model is built in Simulink, as shown in Fig. 21. A controllable voltage source (CVS) is used to simulate the electricity from the photovoltaic power plants. One 200-V/100-kA/20-MW main FCL SC and five 200-V/20-kA/4-MW branch FCL SCs is used to form the FCL SC model system. Five 200-V/20-kA/4-MW resistive loads from load 1 to load 5 are used to simulate the distributed loads located in the terminals from the branch FCL SC 1 to branch FCL SC 5. One second-type 0.06-H/15.5-kA/7.2-MJ SMES A is installed near the bus line between the main FCL SC and branch FCL SCs, while one third-type 0.06-H/15.5-kA/7.2-MJ SMES B is installed near the critical load 1.

The PI section line block is adopted to build an approximate SC circuit model, as shown in Fig. 22. It mainly consists of one distributed inductor with its inductance of $L$, two distributed capacitors with their capacitances of $C/2$, and one equivalent lossy resistor with its resistance of $R(t)$. The cable inductance and cable capacitance

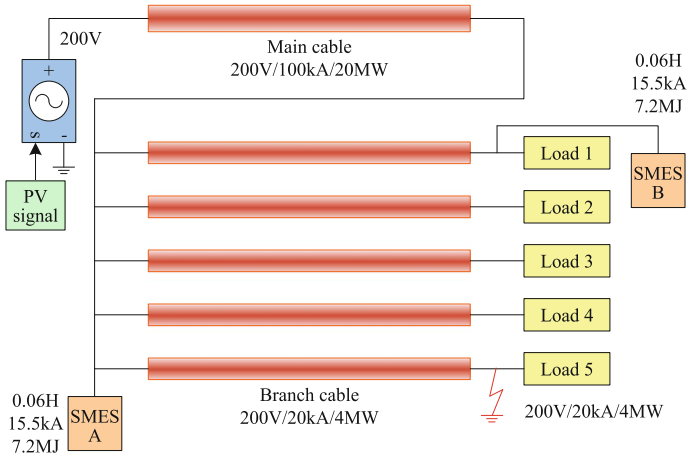


**Fig. 21** Simulation model of the LVDC micro photovoltaic grid

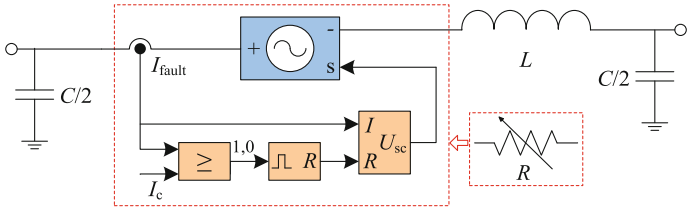


**Fig. 22** FCL SC circuit model

per unit length are 2 mH/km and 8.6 pF/km as standard, respectively. The total lengths of the main cable and each branch cable are 10 and 1 km, respectively.

The lossy resistance characteristic of the SC is similar to the resistive-type superconducting fault current limiter [32]: (i) When the grounding fault current $I_{fault}(t)$ exceeds the critical current $I_c$ of the SC, a quench state starts, and thus $R(t)$ increases exponentially to a maximum value of $R_m$, i.e., $R(t) = R_m \times [1 - \exp(-t/\tau_1)]$; (ii) Subsequently when the grounding fault disappears, a recovery state starts, and thus $R(t)$ decreases exponentially to zero, i.e., $R(t) = R_m \times \exp(-t/\tau_2)$. $\tau_1$ and $\tau_2$ are the time constants of the quench period and recovery period, respectively. The dynamic changes of $R(t)$ ensures the self-acting FCL feature of the SC.

The SMES system is divided into twenty SMES units in parallel, with each unit consists of one 1.2-H/775-A/360-kJ SMES coil unit [33] and one bridge-type chopper unit [15–18], as shown in Fig. 23. The bridge-type chopper is formed by four MOSFETs $S_1$-$S_4$ and two diodes $D_2$, $D_4$. As compared to the conventional chopper formed by two MOSFETs $S_1$, $S_3$ and two diodes $D_2$, $D_4$, the bridge-type one has higher energy utilization efficiency in the LVDC network. To further

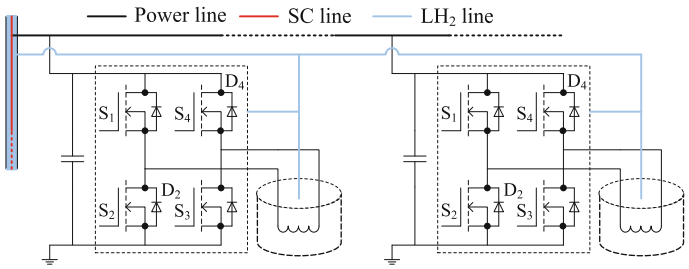


**Fig. 23** SMES circuit model

improve the efficiency, cryogenic MOSFET units cooled by the low-temperature gas hydrogen from the SMES Dewar are the available options. As for the SMES control, all the operation states are digitalized as "$S_1S_2S_3S_4$" by defining the turn-on or turn-off status of a MOSFET as "1" or "0". The charge–storage operation mode ("1010" → "0010" → "0110" → "0010" → "1010") and the discharge–storage operation mode ("0101" → "0100" → "0110" → "0100" → "0101") correspond to the control schemes for the power absorption and compensation operations, respectively.

## *3.3 SMES Coil Design*

To further improve the allowable coil critical current in a solenoidal SMES coil, the simplest method is to adopt two or more parallel pancake coils which served as one coil unit located at two coil ends. However, it needs more tape usage and higher capital cost. A number of feasible optimization methods such as electromagnetic field analyses, simulated annealing algorithm, adaptive genetic algorithm, continuum sensitivity approach, sequential quadratic programming approach are consequently studied for structural optimizations. Among the most literatures related to the coil optimizations, they are aiming to achieve a maximum energy storage capacity with a determined tape usage, or achieve a reference energy storage capacity with a minimum tape usage. For instance, Noguchi et al. [34, 35] propose a steps-shaped cross-sectional shape having several stepped coil units to reduce about 24 % in tape usage. By considering the ratio between the critical current and tape usage in the mentioned optimization methods above, the step-shaped shape has a maximum value. Therefore, it is preferable to achieve a very high critical current with a determined tape usage, and thus used to carry out the conceptual design of the 0.06-H/15.5-kA/7.2-MJ SMES coil in the proposed LVDC micro photovoltaic grid.

The designed coil assembly has 20 1.2-H/775-A/360-kJ solenoidal units in parallel, as shown in Table 2. Each unit is connected to the bus line between the main cable and five branch cables through one bridge-type chopper unit. Critical

**Table 2** Specifications of the magnet assembly and coil units

| Items | Coil unit | Magnet assembly |
|---|---|---|
| Inductance | 1.2 H | 0.06 H |
| Critical current | 880 A | 17.6 kA |
| Rated current | 775 A | 15.5 kA |
| Rated energy | 360 kJ | 7.2 MJ |
| Rated power | 150 kW | 3 MW |
| Rated voltage | 200 V | 200 V |

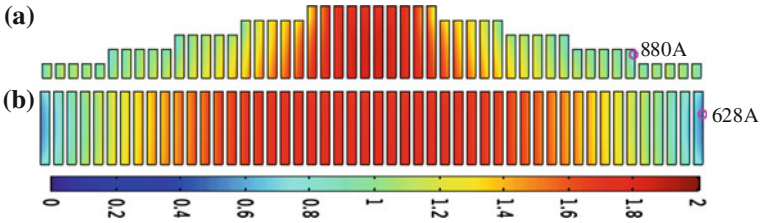


**Fig. 24** Critical current (kA) distributions of **a** *rectangular-shaped* coil and **b** *step-shaped* coil

**Table 3** Specifications of the 1.2 H SMES coil

| $N_{disk}$ | $N$ | $r_{inner}$ (mm) | $r_{outer}$ (mm) | $h$ (mm) | $S_{tape}$ (m) |
|---|---|---|---|---|---|
| 1–5 | 10 | 278 | 285 | 32.5 | 168.2 |
| 6–10 | 20 | 271 | 285 | 32.5 | 336.3 |
| 11–15 | 30 | 264 | 285 | 32.5 | 504.5 |
| 16–20 | 40 | 257 | 285 | 32.5 | 672.7 |
| 20–25 | 50 | 250 | 285 | 32.5 | 840.9 |

current (kA) distributions of the rectangular-shaped coil and the step-shaped coil are shown in Fig. 25 [30, 31]. Benefited from the reduced perpendicular magnetic fields located at two coil ends, the critical current and tape usage requirement of the step-shaped coil are about 1.4 times and 0.6 times of those of the rectangular-shaped coil.

The 1.2 H step-shaped coil can be divided into two axisymmetric left and right parts. Each part consists of five stepped coil units with each unit having five disks, as shown in Fig. 24. The average width $w$ and average thickness $t$ of the used DI-BSCCO tapes are 4.5 and 0.3 mm, respectively. Two stacked tapes are used to wind the coil so as to achieve a high critical current of 880 A at 20 K. The gap between two adjacent turns in the same disk is 0.1 mm. The gap between two adjacent disks is 2 mm. From the right to left of the 50 coil layers, they are defined as $N_{disk} = 1$, $N_{disk} = 2$, …, $N_{disk} = 50$, respectively. Table 3 summarizes the coil turns $N$, inner radius $r_{inner}$, outer radius $r_{outer}$, height $h$, and tape usage $S_{tape}$ of the five stepped coil units.

### 3.4 Performance Evaluation

In the simulations, the three 200-V/10-kA/2-MW resistive loads are connected or disconnected to the cable terminal by controlling the three series-connected breakers. Three operation states of the connected resistive load(s) are consequently achieved: (i) When one of the three breakers closes, the connected resistive load is operated in a power swell state; (ii) When two of the three breakers close, the connected resistive loads are operated in a rated power state; and (iii) When all the three breakers close, the connected resistive loads are operated in a power sag state.

Figure 25 shows the simulated load voltage $U_{load}(t)$ during the power sag period from 0.5 to 3 s. If the SMES system is not applied, the load voltage $U_{load}(t)$ will decrease rapidly to about 183.8 V at 1.5 s and then increase gradually. At the time $t$ = 3 s when two of the three breakers close, $U_{load}(t)$ increases exponentially to about 203.3 V at 3.8 s. In the case of the SMES system is applied, the twenty bridge-type chopper units are operated in the discharge–storage mode to compensate the shortfall power from the bus line. As a result, $U_{load}(t)$ is maintained around its rated voltage with a maximum voltage ripple of about 198.8 V at 3 s. Accordingly, the coil current $I_L(t)$ decreases to about 9.8 kA at 3 s, as shown in Fig. 26.

Figure 27 shows the simulated load voltage $U_{load}(t)$ during the power swell period from 0.5 to 3 s. If the SMES system is not applied, the load voltage $U_{load}(t)$ will increase rapidly to about 218.3 V at 1.6 s and then decrease gradually. At the time $t$ = 3 s when two of the three breakers close, $U_{load}(t)$ decreases exponentially to about 196.1 V at 6 s. In the case of the SMES system is applied, the 20 bridge-type chopper units are operated in the charge-storage mode to absorb the surplus power from the bus line. As a result, $U_{load}(t)$ is maintained around its rated voltage with a maximum voltage ripple of about 201.4 V at 2 s. Accordingly, the coil current $I_L(t)$ increases to about 15.6 kA at 3 s, as shown in Fig. 26. Therefore, the SMES system can protect the load voltage effectively under both power sag and power swell conditions.

To evaluate the fault current limitation (FCL) characteristic of the superconducting cable, an additional breaker is used to simulate a short-circuit fault in the branch cable 5. In the simulations, the cable inductance and cable capacitance per

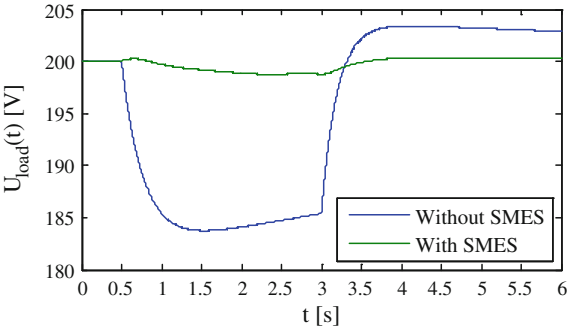


**Fig. 25** Load voltage $U_{load}(t)$ during a power sag period

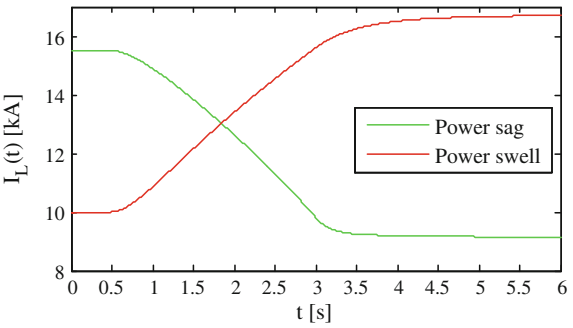


**Fig. 26** Coil current $I_L(t)$ during a power swell period and a voltage sag period

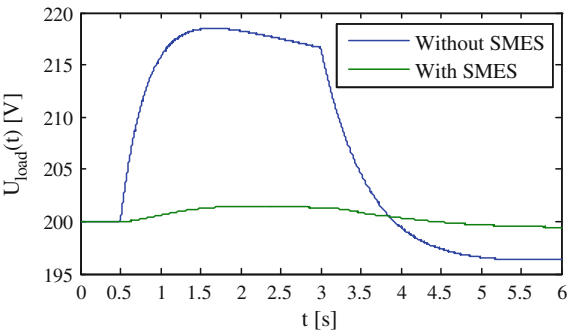


**Fig. 27** Load voltage $U_{load}(t)$ during a power swell period

unit length are set as 2 mH/km and 8.6 pF/km, respectively. The total lengths of the main cable and each branch cable are set as 10 and 1 km, respectively. From the simulation results and analyses under a short-circuit fault condition, the DC SC having the self-acting FCL characteristic can simultaneously protect the load voltage and current of the adjacent branch cables, but there are still unavoidable load voltage and current drops after the fault occurrence. This is because the quenching degree becomes increasingly serious as the fault current rises, and thus the resulting superconducting resistance increases exponentially from zero to a maximum value along with the quenching time.

To achieve a better protection effect, the SMES is applied to cooperate with the DC SC. The basic cooperative operation principle of the FCL SC and SMES is shown in Fig. 28. The FCL SC branch 5, SMES A and SMES B are equivalent to one fault-current-dependent increased voltage source $U_{sc}$ and two load-voltage-dependent decreased current sources ($I_A$, $I_B$), respectively. Two load-voltage-dependent switches ($S_A$, $S_B$) are closed to switch on the SMES A and SMES B when the bus voltage $U_{bus}$ and load voltage $U_{load}$ are lower than their rated values. Thus, the increased $U_{sc}$ offsets the line voltage to limit the fault current through the FCL SC branch 5, while the discharging currents from the SMES A and SMES B prevent the voltage and current drops across the adjacent branch FCL SCs.

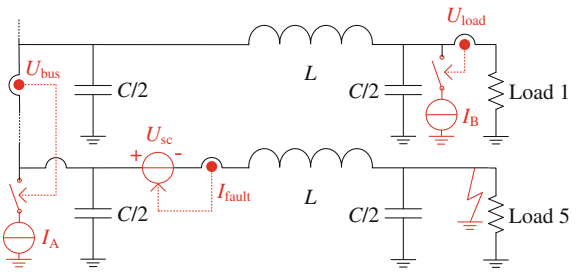


**Fig. 28** Basic cooperative operation principle of the FCL SC and SMES

To further enhance the FRT capability of the in-grid photovoltaic power plants, the SMES A is applied to cooperate with the FCL SC. As shown in Fig. 29a, b, the fault current is significantly limited due to the self-acting FCL resistance $R(t)$, and thus the load voltage $U_{load}(t)$ remains around 200 V from 0.5 to 1 s. This means that the grounding fault has virtually no impact on the adjacent FCL SC branches if the fault time duration is less than 0.5 s. However, if other energy storage systems such as electrochemical cells are applied, their slow start-up time will cause relatively obvious load voltage drop after 0.5 s. From the green line in Fig. 29a, when the start-up time is 25, 50, and 100 ms, the corresponding load voltage reduces to about 198.3, 196.8, and 193.7 V. From 1 to 3 s, $U_{load}(t)$ drops gradually to a minimum value of 180 V and then remains nearly unchanged. Accordingly, the coil current $I_A(t)$ in Fig. 29c decreases to about 8.6 kA at 3 s and then remains unchanged. As compared to the load voltage curve with the FCL function only, the load voltage reduction decreases from 20 to about 10 %.

When the time $t$ = 3 s, the grounding fault removes. The FCL SC branch 5 is still operated in the quench state until $I_{fault}(t)$ decreases to 30 kA at about 3.15 s. After that, a recovery state starts, and $R(t)$ decreases exponentially to zero. Due to the high transient current through the FCL SC branch 5, $U_{load}(t)$ increases rapidly to a maximum value and then decreases to 200 V. With the SMES A, the maximum load voltage after the fault disappearance drops from 210 to about 205 V, and the voltage recovery time reduces from 27 to about 22 s. Therefore, the SMES A has a positive effect on grid voltage stability and enhances the FRT capability.

Although 10 % reduction in the load voltage with the cooperative operation of the FCL SC and SMES A is enough to achieve the practical FRT of the in-grid photovoltaic power plants, it is not allowed by the critical load 1 located in the terminal of the branch FCL SC 1. To obtain a longer voltage protection time duration, the SMES B installed near the critical load 1 should be applied after the time $t$ = 1 s. As shown in Fig. 30a, the load voltage $U_{load1}(t)$ through the FCL SC branch 1 can further maintain around 200 V for about 4 s. Due to the existence of an inevitable control system time delay including a sampling time of the load voltage, a computing time of the digital control system, and an on-off implementing time of the MOSFETs, the practical control signals for the SMES charge–discharge

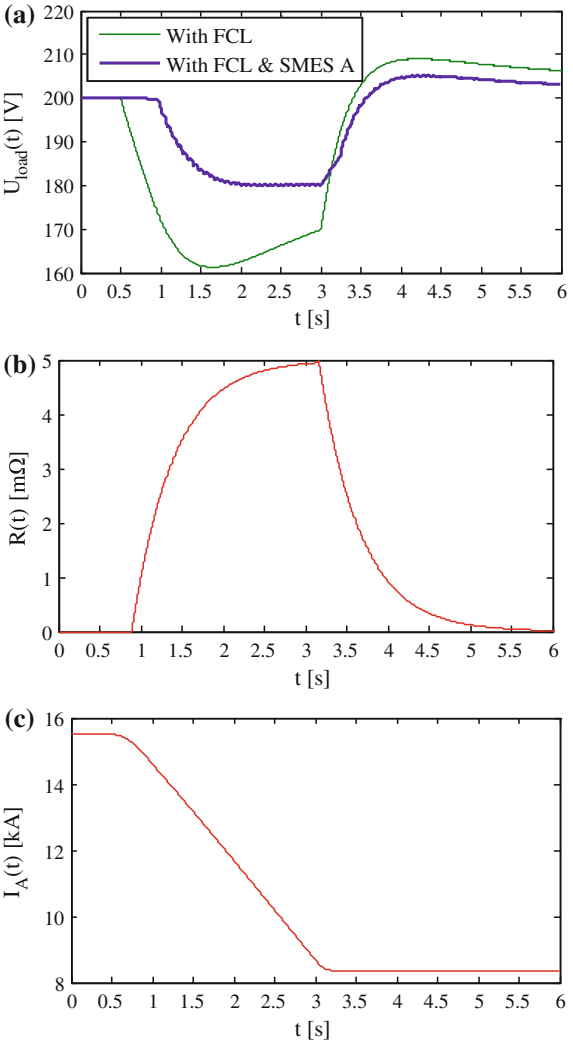


**Fig. 29** Simulated results during a grounding fault: **a** $U_{load}(t)$ versus $t$; **b** $R$ $(t)$ versus $t$; (c) $I_A(t)$ versus $t$

operation lag behind the changes of the load voltage. This will result in some undesired voltage overshoots accordingly. In addition, with the cooperative operation of the SMES A and SMES B, the minimum load voltage $U_{load2}(t)$ through the FCL SC branch 2 increases from 180 to about 184 V. Accordingly, the coil currents $I_A(t)$ and $I_B(t)$ decreases to 2.3 and 9.5 kA at 5 s, as shown in Fig. 30b.

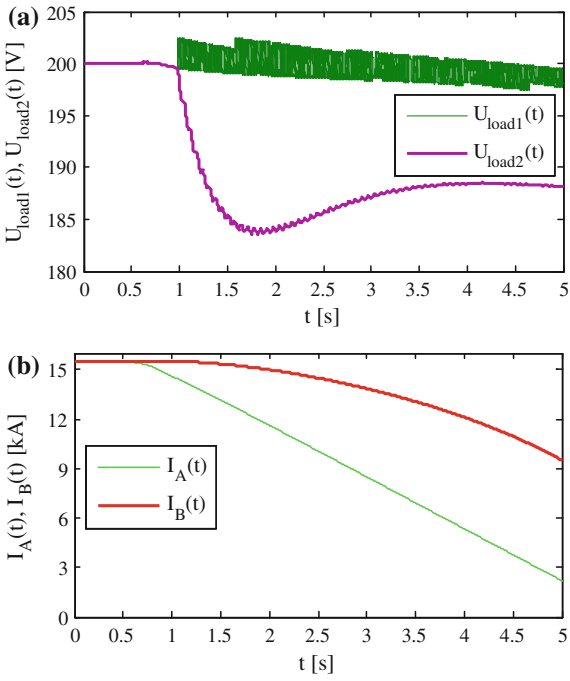


**Fig. 30** Simulated results with the cooperative operations of FCL SC branch 5, SMES A and SMES B: **a** $U_{load1}(t)$, $U_{load2}(t)$ versus $t$; **b** $I_A(t)$, $I_B(t)$ versus $t$

## 4 Summary and Application Prospect

In most smart grid plans integrated with photovoltaic power plants, one of the most principal development goals is to intelligently supply the highly customizable electricity with high quality and reliability. Due to the rapid load fluctuations from the power end-users and intermittent power fluctuations from the photovoltaic power plants, various ESSs are expected to integrate into the power generation, transmission, distribution, and utilization systems to achieve a good supply–demand balance. They are controlled to absorb the surplus electricity when a power swell occurs, and to release the shortfall electricity when a power sag occurs. The overview and application analyses of the current SMES technology conclude that SMES with the outstanding advantages of fast response speed, high power density, and high storage efficiency has the significant potentials to combine with, even replace other conventional ESSs in the modern power system and future smart grid. It can be well expected that the future SMES devices are not only essential to improve the power quality with small-scale or medium-scale energy storage capacity but also ensure the daily load leveling and overall reliability of the power systems with large-scale energy storage capacity.

The main SMES application schemes and their basic functions are as follows: (i) SMES devices installed near the large-scale centralized generators (CGs) are used to balance the output power and to achieve daily load leveling; (ii) SMES

devices installed in the transmission lines (TLs) are used to form FACTS devices for compensating the load fluctuations and maintaining the grid frequency stability; (iii) SMES devices installed in the distribution lines (DLs) are used to form DFACTS devices for improving the power quality; (iv) SMES devices installed near the distributed generators (DGs) are used to reduce the impacts from the intermittent renewable energy sources so as to facilitate the grid integration; and (v) SMES devices installed near the power end-users are used to form SMES-based UPSs for protecting the critical loads. In the above five application schemes, a number of SMES devices are distributed in the multiarea interconnected networks with the same voltage level on the one hand, on the other hand, they are also distributed in the multivoltage-level interconnected networks including the CGs, TLs, DLs, DGs, and end-users. Therefore, SMES devices in future smart grid integrated with photovoltaic power plants are expected to intelligently handle with the external power exchange demands through the joint efforts with each other.

Besides the sole SMES scheme with full energy storage scale, three feasible application schemes of SMES should also be considered. The sole SMES scheme has one advantage of high storage efficiency for large-scale energy storage, while it has two advantages of fast response speed and high power density for small-scale energy storage. But both the large-scale and small-scale SMES devices are suffered from high capital cost as compared to other commercial ESSs with the same capacity. The SMES-based hybrid energy storage system (HESS) scheme reduces the required energy storage capacity of SMES, but the practical system topologies and relevant control strategies of HESS are more complex over the sole SMES. The distributed SMES (DSMES) scheme has two advantages of high mobility and high expandability because the DSMES units in the trucks are easy to install in arbitrary locations once they arrive on site. To achieve efficient stability and reliability of the whole power system, various distributed HESS (DHESS) units with different energy storage capacities and power ratings should be installed in the power generation, transmission, distribution, and utilization systems. The novel concept of SMES-based HESS scheme utilizes various energy storage technologies efficiently and thus enhances the flexibility and economy of SMES greatly in future photovoltaic power plants. With the rapid development and research of superconducting materials and superconducting power applications, emerging SMES systems and devices have promising potentials to replace or cooperate with other commercial energy storage systems on the one hand; on the other hand, they are also well expected to integrate with other superconducting power devices such as superconducting generator, superconducting cable, superconducting transformer, and superconducting fault current limiter, with essential aims to develop various high-performance, high-efficiency, and high-economy photovoltaic power plants in future smart grid.

## References


1. Castillo A, Gayme DF (2014) Grid-scale energy storage applications in renewable energy integration: a survey. Energy Convers Manag 87:885–894
2. Vazquez S, Lukic SM, Galvan E, Franquelo LG, Carrasco JM (2010) Energy storage systems for transport and grid applications. IEEE Trans Industr Electron 57(12):3881–3895
3. Bradbury K (2010) Energy storage technology review. Duke University
4. Kondoh J, Ishii I, Yamaguchi H, Murata A, Otani K, Sakuta K, Higuchi N, Sekine S, Kamimoto M (2000) Electrical energy storage systems for energy networks. Energy Convers Manag 41(17):1863–1874
5. Yoon JY, Lee SR, Hwang IT (2013) A quantitative analysis on future world marketability of HTS power industry. IEEE Trans Smart Grid 4(1):433–436
6. Jin JX, Xin Y, Wang QL, He YS, Cai CB, Wang YS, Wang ZM (2014) Enabling high-temperature superconducting technologies toward practical applications. IEEE Trans Appl Supercond 24(5):5400712
7. von Helmolt R, Eberle U (2007) Fuel cell vehicles: status 2007. J Power Sources 165:833–843
8. Durbin DJ, Malardier-Jugroot C (2013) Review of hydrogen storage techniques for on board vehicle applications. Int J Hydrogen Energy 38:14595–14617
9. Stekly ZJJ (1963) Magnetic energy storage using superconducting coils. In: Proceedings of pulse-power conference, pp 53
10. Peterson HA, Mohan N, Boom RW (1975) Superconductive energy storage inductor-converter units for power system. In: IEEE Trans Power Appar Syst PAS-94(4):1337–1346
11. Ali MH, Wu B, Dougal RA (2010) An overview of SMES applications in power and energy systems. IEEE Trans Sustain Energy 1(1):38–47
12. Jin JX (2011) High temperature superconducting magnetic energy storage: principle and applications. Science Press, Beijing
13. Jin JX, Chen XY (2012) Study on the SMES application solutions for smart grid. Phys Procedia 36:902–907
14. Chen XY, Jin JX, Xin Y, Shu B, Tang CL, Zhu YP, Sun RM (2014) Integrated SMES technology for modern power system and future smart grid. IEEE Trans Appl Supercond 24 (5):3801605
15. Zhang JY, Jin JX, Chen XY, Zhou X, Ren AL, Gong WZ, Xin Y (2014) Electric energy exchange and applications of superconducting magnet in an SMES device. IEEE Trans Appl Supercond 24(3):5700704
16. Chen XY, Jin JX, Xin Y, Guo YG, Xu W, Wen L, Zhu JG (2014) Energy exchange experiments and performance evaluations using an equivalent method for a SMES prototype. IEEE Trans Appl Supercond 24(5):5701005
17. Jin JX, Xu W, Chen XY, Wen L, Wang SC (2014) Flux flow loss of HT-SMES coil during energy exchange. IEEE Trans Magn 50(11):9000604
18. Jin JX, Chen XY, Wen L, Wang SC, Xin Y (2015) Cryogenic power conversion for SMES application in a liquid hydrogen powered fuel cell electric vehicle. IEEE Trans Appl Supercond 25(1):5700111
19. Jin JX, Chen XY, Qu R, Xin Y (2015) A superconducting magnetic energy exchange model based on circuit-field-superconductor coupled method. IEEE Trans Appl Supercond 25 (3):5700906
20. Grilli F, Pardo E, Stenvall A, Nguyen DN, Yuan W, Gömöry F (2014) Computation of losses in HTS under the action of varying magnetic fields and currents. IEEE Trans Appl Supercond 24(1):8200433
21. Hamajima T, Amata H, Iwasaki T, Atomura N, Tsuda M, Miyagi D, Shintomi T, Makida Y, Takao T, Munakata K, Kajiwara M (2012) Application of SMES and fuel cell system combined with liquid hydrogen vehicle station to renewable energy control. IEEE Trans Appl Supercond 22(3):5701704

22. Shim JW, Cho YH, Kim SJ, Min SW, Hur K (2013) Synergistic control of SMES and battery energy storage for enabling dispatch ability of renewable energy sources. IEEE Trans Appl Supercond 23(3):2062–2065
23. Wen L, Jin JX, Chen XY, Jiang L (2014) A universal LabVIEW-based HTS device measurement and control platform and verified through a SMES system. IEEE Trans Appl Supercond 24(5):9002705
24. Luongo CA, Baldwin T, Ribeiro P, Weber CM (2003) A 100 MJ SMES demonstration at FSU-CAPS. IEEE Trans Appl Supercond 13(2):1800–1805
25. Shikimachi K, Hirano N, Nagaya S, Kawashima H, Higashikawa K, Nakamura T (2009) System coordination of 2 GJ class YBCO SMES for power system control. IEEE Trans Appl Supercond 19(3):2012–2018
26. Sander M, Gehring R, Neumann H (2013) LIQHYSMES—A 48 GJ toroidal $MgB_2$-SMES for buffering minute and second fluctuations. IEEE Trans Appl Supercond 23(3):5700505
27. Grant PM (2005) The SuperCable: dual delivery of chemical and electric power. IEEE Trans Appl Supercond 15(2):1810–1813
28. Jin JX (2007) High efficient DC power transmission using high-temperature superconductors. Physica C 460–462:1443–1444
29. Yamada S, Hishinuma Y, Uede T, Schippl K, Yanagi N, Mito T, Sato M (2010) Conceptual design of 1 GW class hybrid energy transfer line of hydrogen and electricity. J Phys Conf Ser 234:032064
30. Jin JX, Chen XY, Qu R, Fang HY, Xin Y (2015) An integrated low-voltage rated HTS DC power system with multifunctions to suit smart grids. Physica C (Amsterdam, Neth) 510:48–53
31. Jin JX, Chen XY (2015) Cooperative operation of superconducting fault-current-limiting cable and SMES systems for grounding fault protection in a LVDC network. IEEE Trans Ind Appl 51(6):5410–5414
32. Ngamroo I, Karaipoom T (2014) Cooperative control of SFCL and SMES for enhancing fault ride through capability and smoothing power fluctuation of DFIG wind farm. IEEE Trans Ind Appl 24(5):5400304
33. Chen XY, Jin JX (2014) Evaluation of step-shaped solenoidal coils for current-enhanced SMES application. IEEE Trans Appl Supercond 24(5):4603404
34. Noguchi S, Yamashita M, Yamashita H, Ishiyama A (2001) An optimal design method for superconducting magnets using HTS tape. IEEE Trans Appl Supercond 11(1):2308–2311
35. Noguchi S, Yamashita H, Ishiyama A (2002) An optimal design method for SMES coils using HTS tapes. IEEE Trans Appl Supercond 12(1):1459–1462